

This is a postprint version of the following published document:

Pernas-Sánchez, J., Artero-Guerrero, J., Varas, D., López-Puente, J. (2020). Artificial bird strike on Hopkinson tube device: Experimental and numerical analysis. *International Journal of Impact Engineering*, v. 138, 103477, pp.: 1-13.

DOI: <https://doi.org/10.1016/j.ijimpeng.2019.103477>

©2019 Elsevier B.V. All rights reserved.



This work is licensed under a [Creative Commons AttributionNonCommercialNoDerivatives 4.0 International License](https://creativecommons.org/licenses/by-nc-nd/4.0/).

# Artificial bird strike on Hopkinson tube device: experimental and numerical analysis

J. Pernas-Sánchez<sup>a,\*</sup>, J. Artero-Guerrero<sup>a</sup>, D. Varas<sup>a</sup>, J. Lopez-Puente<sup>a</sup>

<sup>a</sup>*Department of Continuum Mechanics and Structural Analysis, University Carlos III of Madrid, 28911 Leganés, Madrid, Spain*

---

## Abstract

This work shows a combined experimental-numerical research in bird impact. In order to perform the experimental tests, a artificial bird has been prepared and impacted against a Hopkinson tube in a wide range of impact velocities (70-200 m/s). The Hopkinson tube was designed in order to measure the induced force transmitted in the tube by the impact. This force could be used to compare different experimental tests and also to validate the numerical models proposed. In addition, the whole process of impact was recorded by means of high speed video cameras. The images captured allow to perform the analysis of the bird kinematics during the impact. Numerically, in order to reproduce the high deformations experienced by the artificial bird in the impact process, the Smooth Particle Hydrodynamics (SPH) technique has been used. Concerning the artificial bird material behaviour, four different models were employed, combining the two material models and two equations of state most used in the literature. The four cases have been compared with the experimental measurements and benchmarked. After the analysis of the results, it can be concluded that the combined experimental-numerical methodology proposed successfully can be used to study and validate the numerical models for simulating the behaviour of soft impactor when subjected to high velocity impacts. It can be seen that the normal impact forces induced by the impact are reproduced adequately for all the numerical models. However the radial spreading of the soft impactor is not reproduced as adequately as the other cases, especially in low velocity impacts. This effect can be important to reproduce the radial distribution of pressures and the secondary impacts produced by this radial expansion.

*Keywords:* Bird strike, Experiments, Numerical simulations, Gelatine bird artificial, artificial bird, impact, Material models, SPH, Soft body impact, secondary impact

---

---

\*Corresponding author: [jpernas@ing.uc3m.es](mailto:jpernas@ing.uc3m.es)

## 1. Introduction

Industries such as aeronautic and aerospace permanently seek to optimize structural components due to the high requirements demanded to the aircrafts for both safety and reliability. Moreover these industries are continuously improving their structures in order to reduce the weight of the aircraft, which matches with the social challenge of achieving a more sustainable transport. These improved structures should withstand severe cases of loads to accomplish the certification requirements; traditionally the designers use experimental tests to validate it. The high cost of the experimental tests leads engineers to implement numerical tools, for which appropriate material models are required in order to produce accurate results. Therefore obtaining experimental data reliable to validate material models are a key point for the engineers.

Test load cases for aeronautic structures are extensive but among others, impact is one of the most concerning loads to which an structure is subjected. Different elements could impact on the structure during the landing and take-off operations, which can lead to damages in the structures. Events such as the US Airways Flight 1549 in which after the struck of a Canada geese flock, the plane suffered several damages losing all engine power and finally landing in the Hudson river; or the case of Concorde that due to a tyre impact one of the fuel containers caught fire; are examples in which such type of loads promotes the lost of structural integrity. This menace has been reported by the authorities: literally from an EASA 2011 report “*A critical safety issue for the design of primary aircraft structures is vulnerability and damage tolerance due to foreign object impact from bird strike, hail, tyre rubber and metal fragments*”, [1] highlighting the impact threat as a key factor in the design of composite structures.

Several authors have studied such type of events, from an experimental and a numerical point of view, using different types of impactors. The impacts caused by quasi-non-deformable bodies (metal fragments), or highly deformable (hail, bird), have been studied in some depth [2, 3, 4, 5, 6]. But as the material models increase in complexity to capture the physics of the impactor requires extensive experimental data, which is difficult in the case of highly deformable materials subjected at high strain rates. These impactors flow over the structure, spreading the impact load; thus for accurate damage prediction in aeronautical structures it is necessary to obtain appropriate experimental data to develop reliable modelling techniques for both impactor and target.

Extensive experimental work has been done during the decade of 70’s. In the work of Willbeck et al.[7], bird (from 0.1 kg to 4 kg), gelatin (with several values of porosity), porous RTV rubber and beef steak have been launched in a range of approximately 100-300 m/s against a Hopkinson bar to measure the impulse and pressure induced during the impact. Other methodologies have been used to measure the impact forces

32 induced by the impact such as a piezoelectric force transducer [8]. Also the impulse and the average force  
33 can be measured tracking the velocity of the impacted structure when is mounted on a frictionless rail [9]  
34 or using hopkinson tubes as in the present research [10].

35 Concerning the impact on aerospace structures, there are several works in which experimental and  
36 numerical methodologies have been combined to deepen the comprehension of the problem. It has to be  
37 remarked the work of Liu et al. [11] in which both experimental and numerical results of a tail leading edge  
38 being impacted by a 3.6 kg bird are presented. Hu et al. [12] performed an experimental test to analyze the  
39 impact resistance of a composite helicopter cockpit. A numerical simulation was used to improve the design  
40 of the cockpit. Also aluminum plates, impacted against bird, are studied in the work of Liu et al. [13]. The  
41 predicted displacement, strain in the plates and impact reaction forces of experimental tests are compared  
42 with the numerical results showing a good correlation between them.

43 Regarding the numerical methodologies used, the most suitable ones are the techniques which are able  
44 to deal with large deformation, contact and non-linear behaviour of materials such as the Eulerian, the  
45 Arbitrary Lagrangian Eulerian (ALE) or the Smooth Particle hydrodynamics (SPH) approaches. This last  
46 method is one of the most used in the literature because of its good correlations with experimental results  
47 [14, 15, 16, 17, 18, 19, 20]. Recently it has been published the work of A. Riccio et al. [21] where four different  
48 numerical approaches to model the bird (Rigid, Lagrangian, SPH and Coupled Eulerian Lagrangian (CEL))  
49 have been presented and compared for the same bird mass, velocity, and boundary conditions. It has been  
50 shown that both CEL and SPH seem to provide the most realistic results. Also Siemann et al. [22] study  
51 the influence of the particle distribution in the pressure contact, using a Weighted Voronoi Tessellation  
52 algorithm, obtaining an improvement in the pressure peaks distributions respect to the reference particle  
53 distribution.

54 In this work, a combined experimental-numerical methodology is presented to validate material models  
55 subjected at high impact velocity; applying it to a real case of study: the bird impact. Instead of using  
56 real birds for the experimental campaign, artificial birds (AB) made from gelatin are employed, avoiding  
57 the spread of properties related to the different bird species. The AB are launched against a Hopkinson  
58 tube in order to measure the deceleration and the stress pulse generated in the tube at different impact  
59 velocities. The kinematics of the impactor was captured by means of high speed cameras. The results  
60 obtained have been used to validate numerical models for the bird proposed in the literature, proving the  
61 combined experimental-numerical methodology. It is particularly emphasized the radial expansion of the  
62 artificial bird; phenomenon that, as can be seen, all the numerical models fail to reproduce adequately.

63 In addition the experimental results from the Hopkinson tube, which are shown, can contribute to the  
64 development of simulated bird behaviour models by other researchers.

---

65

## 66 2. Experimental setup

67 In this section the experimental techniques used to perform the impacts tests are explained. First the  
68 manufacturing of artificial bird and later the facilities used are detailed.

### 69 2.1. Artificial bird preparation

70 There are a high amount of bird species, with an average mass and a specific shape, that can impact  
71 against an aeronautic structure. Hamershock et al. [23] recollected data from different bird species and  
72 specimens obtaining the average mass and contour diameter of each one. Figure 1 shows the results of the  
73 study, it can be observed that as the bird mass increases the density measured decreases, while the inverse  
74 trend regarding the contour diameter can be observed. The study not only shows the dispersion of bird  
75 species, but the differences between specimens of the same specie. In order to reduce the uncertainty, some  
76 institutions and researchers [7, 24, 25] propose a artificial bird made of gelatine, which is the approach used in  
77 the present study. A recipe to obtain 1 kg of gelatine can be found in Lavoie et al. [25], where the amounts  
78 of ingredients and procedure are detailed. In the present study a simpler recipe for the artificial bird is  
79 proposed, just using water and ballistic gelatine powder; the procedure and times are given in table 1. The  
80 gelatine employed, “250 Type A Ordnance Gelatin” from Gelita<sup>®</sup>, was selected because it is recommended  
81 to reproduce the mechanical behaviour of organic tissues under ballistic conditions. The selected mass for the  
82 present study is around 355 g, representing a laughing gull or a rocking dove. Following the statistical data  
83 obtained by Hammershock et al. [23], the density of the gelatine should be around  $1 \text{ g/cm}^3$  and the contour  
84 shape  $\sim 57 \text{ mm}$  (figure 1). Finally, the selected geometry of the AB was cylindrical with hemispherical caps  
85 of 56.5 mm of diameter and 160 mm long as it is presented in the work of Budgey [24], which gives an aspect  
86 ratio of  $L/D \sim 2.8$ . This geometry is a common simplification of a real case impact scenario in the research  
87 community [24, 25, 26], some authors explore the implications of using an accurate bird shape modeling  
88 showing the influences in the induced force [27].

89 The shape of the impactors is obtained pouring the gelatine into a mould designed and manufactured  
90 using 3D print process, giving as a result a AB of  $355 \pm 4 \text{ g}$  with an average density of  $1.01 \pm 0.01 \text{ g/cm}^3$ .  
91 The selected contour and density are depicted using a black marker in figure 1, it can be observed how

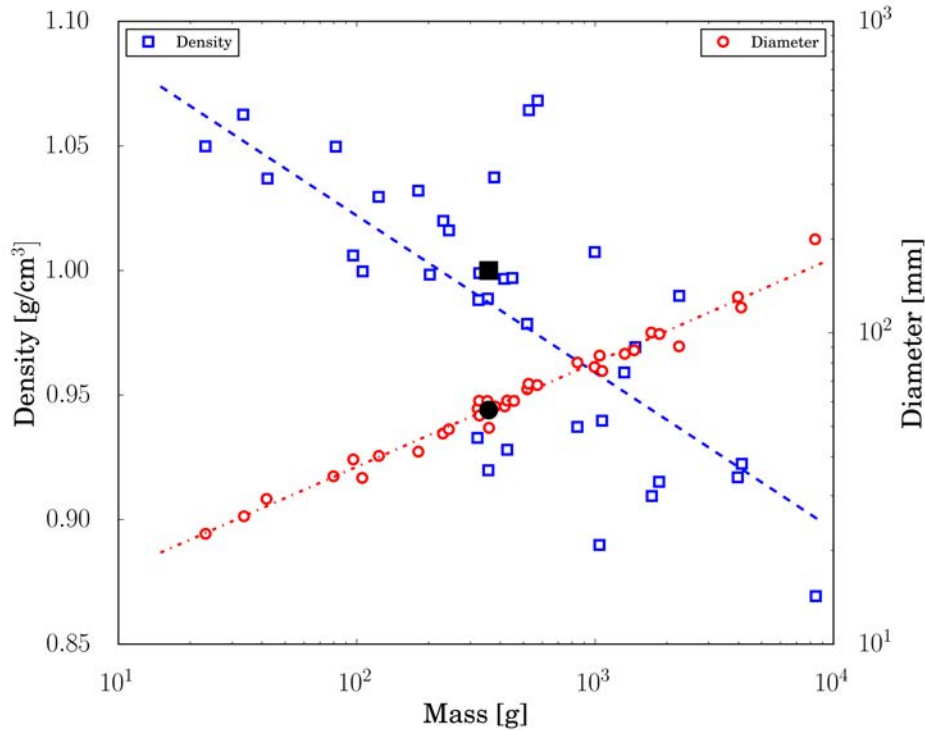


Figure 1: Diameter density mass [23, 24]

92 the values matches with the trends for the different bird species. All the projectiles were conserved at 5°C  
 93 before the impact assuring a constant temperature in all the tests.

94 *2.2. Impact tests*

95 In order to accelerate the artificial bird (AB), a one stage light gas gun was employed, which uses  
 96 pressurized air (or helium) to impel the projectile through 20 meters long, 60 mm calibre barrel (Figure  
 97 2). The impact velocity, in the range between 70-200 m/s, was measured by means of a laser sensor placed  
 98 between the barrel muzzle and the target. These laser barriers were also used to trigger the high speed  
 99 cameras and the high speed data acquisition system (Dewetron DEWE-800), similar facilities were used in  
 100 a previous work of the authors [5]. The gap between the air gas gun calibre (60 mm) and the AB diameter  
 101 (56.5 mm) allows to use a sabot, which avoids friction during the acceleration in the barrel and maintains  
 102 the AB shape. This sabot was 3D printed and designed in order to be deflected by aerodynamic drag  
 103 forces, avoiding its impact on the target. The impact process was recorded using two Photron SA-Z high  
 104 speed cameras configured at 20000 frames per second (the shutter selected was 1/100000 s in order to have  
 105 images without blur) with a resolution of 1024×1024 pixels; one was located perpendicularly to the impact  
 106 plane in order to check the impact velocity and analyse the impact process. The other camera was used

---

Ingredients:

- 909.1 g distilled water.
- 90.9 g ballistic gelatine powder.

---

Procedure:

1. Weighting: Prior to manufacture the AB it is necessary to weight the amount of distilled water and dry gelatine, according to the percentage of dry gelatine to be used (increase the % of gelatine powder may vary the final density and strengths)
2. Add the gelatine powder to the cold distilled water, stirring during the process. The stirring should be done avoiding bubbles. The resulting mix must be opaque and granular.
3. Rest 10 min.
4. Warm the mix between 45° and 55°C. Avoid temperatures higher than 60°C due to this temperature degrades the mix. During the warming try to avoid stirring the mix.
5. Rest the mix during the cool. The mix should be transparent.
6. Prior to acquire 40°C the mix must be pour into the mould.
7. Cool the mould with the mix into the freezer at -18°C during 2 h and 30 min.
8. Keep the artificial bird in the refrigerator between 4° and 15°C, during almost 1 day before testing.

---

Table 1: Gelatine preparation procedure

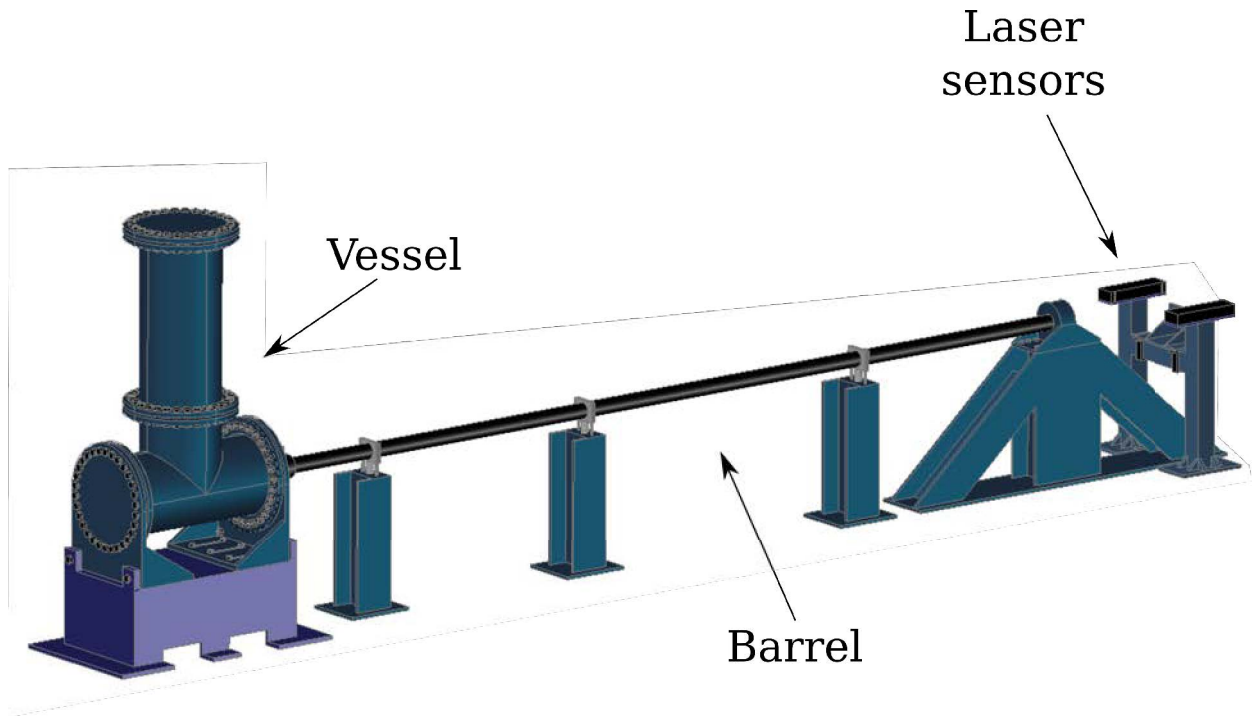


Figure 2: One stage air gas gun used for impel the projectile in uc3m facilities

107 to visualize the impact and confirm the validity of the test in terms of impact location. The lighting was  
 108 provided by means of two Arrisun HMI lamps of 1800 W. The force signal induced by the artificial bird  
 109 impact was measured using a Hopkinson tube. This apparatus was designed long enough to measure large  
 110 pulses of small forces. Based on this premise it has been selected 6 m long, with a tubular cross section  
 111 of 80 mm diameter and 2mm of thickness made of Aluminium AW6060-T66. At both ends of the tube,  
 112 a steel plate (200 mm diameter and 25 mm thickness) was attached being able to be used as a target for  
 113 the impactor. Finally, the tube was instrumented with strain gauges disposed as a Wheatstone bridge at  
 114 350 mm from the impact point. The strain signals were stored by the data acquisition system (Dewetron  
 115 DEWE-800) with a sample rate of  $1 \cdot 10^6$  data per second. The strain gauges were manufactured by Vishay  
 116 Micro-Measurements, item code MMF003129 with a  $350 \pm 0.3\% \Omega$ . The isolation between each strain gauge  
 117 and the Hopkinson tube was checked prior to the tests using a Vishay gage installation tester 1300. Similar  
 118 facilities were employed by the NASA and other researchers for impact test measurement [6, 10]. Finally,  
 119 the Hopkinson tube was aligned with the projectile trajectory using laser leveling to assure a frontal impact  
 120 against the facility. The tube was suspended in order to avoid any restriction and to keep the 1-D nature of  
 121 the facility. Normal impact was selected due to it has been considered the most dangerous impact case [28].  
 122 Using these facilities, 14 different AB projectiles were tested at different velocities ranging from 70 to 200

Test	AB mass [g]	Impact velocity [m/s]	Number of repetition
1	360	75	3
2	355	100	2
3	360	120	3
4	355	150	2
5	360	175	2
6	360	200	2

Table 2: Tests summary

123 m/s (Table 2), all the impact velocities were tested at least 2 times in order to assure a good repeatability  
124 (The number of repetition performed is depicted in table 2).

### 125 *2.3. Modal analysis characterization*

126 In addition to the artificial bird impacts, a modal analysis of the Hopkinson tube was performed. To  
127 this end, the modal frequencies of the Hopkinson tube were measured by means of an accelerometer and  
128 an instrumented hammer (Accelerometer: PCB Piezotronics model 352C33; Hammer: PCB Piezotronics  
129 model 086C03). The hammer impacted at the same location of the AB and the accelerometer measured the  
130 response of the tube under the hammer impact in the longitudinal axis, obtaining the frequency response  
131 of the structure, and hence its modal frequencies. The results of these tests were employed to validate the  
132 numerical model of the Hopkinson tube.

## 133 **3. Numerical modelling**

134 The numerical model developed for the impact of a artificial bird on a Hopkinson tube was implemented  
135 in LS-Dyna v.971-R10. The Hopkinson tube was modelled using hexaedral solid elements, while a mesh-free  
136 approach (Smooth Particle Hydrodynamic SPH) was used for the modelling of the AB. In this section both  
137 approaches are detailed.

### 138 *Numerical model of the Hopkinson Tube*

139 The Hopkinson tube has been modelled by 3 different parts (as in the experimental setup): one aluminium  
140 tube, two steel plates attached to both ends of the tube. All the parts are modelled using solid elements  
141 with elastic materials, due to no plastic deformation was observed after the impact tests, the properties and  
142 the number of solid elements used in each part are depicted in table 3.

143 The discretization used was obtained after a mesh convergence iteration using the experimental modal  
144 frequencies as a benchmark. The different components of the facility have been attached using a contact

Part name	Material	Density ( $\rho$ ) [ $kg/m^3$ ]	Young Modulus ( $E$ ) [ $GPa$ ]	Poisson ratio ( $\nu$ )	Elements
Tube	Aluminium 6060-T66	2500	70.6	0.28	6400
Steel plates	Mild steel	7850	210	0.3	15776

Table 3: Material properties and discretization of the Hopkinson tube

Experimental	Numerical	Error %
164	180,18	9,8
470	517	11
838	931	11,1
1220	1365	11,2
1620	1804	11,1
2020	2244	11,1

Table 4: Experimental and numerical longitudinal modal frequencies of the Hopkinson tube

145 tied formulation. As it was said previously, in the experimental test only longitudinal modes are obtained,  
 146 therefore it has been restricted the displacement of several nodes avoiding the flexural modes.

147 The results from the modal analysis of the Hopkinson tube obtained experimental and numerically are  
 148 compared in Table 4. The table 4 shows the first 6 longitudinal modal frequencies of the tube; all the  
 149 frequencies are faithfully predicted by the numerical simulations, the errors associated by the numerical  
 150 predictions are around 10 %. Taking into account the numerical results of the modal analysis of the  
 151 Hopkinson tube it is possible to state that the mesh refinement is appropriate to be used for the numerical  
 152 model of the Hopkinson tube, at least for longitudinal phenomenon.

### 153 *Numerical model of the artificial bird impact*

154 The numerical simulations of the artificial bird impact use the aforementioned Hopkinson tube model,  
 155 but in this case the AB impactor is included and the explicit module of LS-Dyna has been employed. The  
 156 complete numerical model can be observed in figure 3. The AB was defined using the smooth particle  
 157 hydrodynamics technique, this mesh-free approximation was selected due to the large deformation suffered  
 158 by the AB during the impact. In this case, an eulerian kernel with renormalization technique is used for  
 159 the SPH method [29, 30] in order to deal with large deformations having a precise modelling of the material  
 160 surfaces. After a mesh convergence study, the number of elements used for the artificial bird were 15872  
 161 particles. The smooth length of the particles was 1.2 times the particle radii.

162 In order to define the constitutive behaviour of bird, in this work two different equation of state and two  
 163 different deviatoric models are used, resulting in four different approaches that are used and benchmarked.

164 Concerning the deviatoric material models:

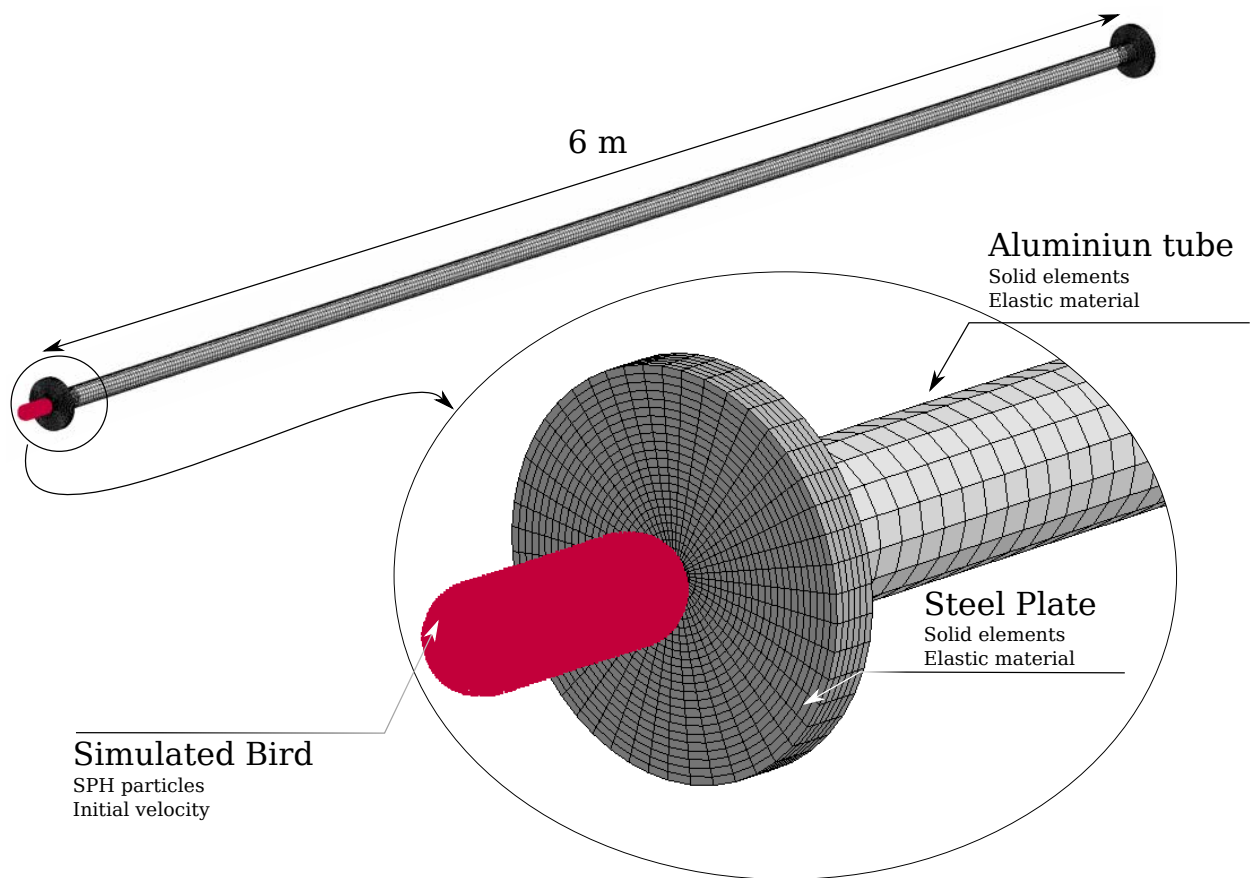


Figure 3: General mesh including the AB discretized using SPH

165 • *Fluid-like material*: the constitutive behaviour was modelled using a fluid-like behavior in which the  
 166 deviatoric stress tensor is defined linearly with the dynamic viscosity ( $\eta$ ) being  $\dot{\varepsilon}'$  the deviatoric strain  
 167 rate tensor.

$$168 \quad s = 2\eta\dot{\varepsilon}' \quad (1)$$

169 • *Isotropic elastic plastic hydrodynamic material (IEPH)*: this model was proposed and used for numer-  
 170 ical simulations by other authors [25, 31, 32] in which it is defined a yield stress ( $\sigma_0$ ) and a linear  
 171 plastic regime characterized by the plastic hardening modulus ( $E_h$ ).

$$172 \quad \sigma_y = \sigma_0 + E_h \bar{\varepsilon}_p \quad (2)$$

173 The material parameters used in the simulations for both materials are depicted in table 5.

174 Concerning the equation of state:

175 • *Polynomial EOS*: this case relates the pressure  $P$ , the density  $\rho$  and the initial density  $\rho_0$  as:

$$176 \quad P = C_1 \left( \frac{\rho}{\rho_0} - 1 \right) \quad (3)$$

177 being  $\rho$  the current material density and  $\rho_0$  being the initial density and  $C_1 = 2.25 \cdot 10^3$  [MPa] a  
 178 material constant. The material properties were obtained from the literature [33].

179 • *Murnaghan EOS*: this EOS relates the pressure  $P$ , the density  $\rho$  and the initial density  $\rho_0$  as:

$$180 \quad P = k_0 \left( \left( \frac{\rho}{\rho_0} \right)^\gamma - 1 \right) \quad (4)$$

181 where the material parameters  $k_0 = 128$  [MPa] and  $\gamma = 7.98$  were identified using a optimization  
 182 algorithm by McCarthy et al. [34].

183 A comparison between both equations of state is shown in figure 4, it can be observed that for low relative  
 184 densities the Murnaghan equation predicts lower values (relative density lower than 1.22) of pressure but is  
 185 more sensitive against increases of relative densities.

186 The EOS is also related to the sound velocity ( $c = \sqrt{\frac{\partial P}{\partial \rho}}$ ). Therefore in case that the impact may not  
 187 induce a sufficient compressive state (relative density lower than 1.12) the Murnaghan EOS will produce a

Parameter	Value
Dynamic viscosity	$\eta = 10^{-3} Pa s$
Shear Modulus	$G = 2.07 GPa$
Yield stress	$\sigma_0 = 0.02 MPa$
Plastic modulus	$E_H = 0.001 MPa$

Table 5: Bird material properties for the fluid-like material and the isotropic elastic plastic hydrodynamic material model

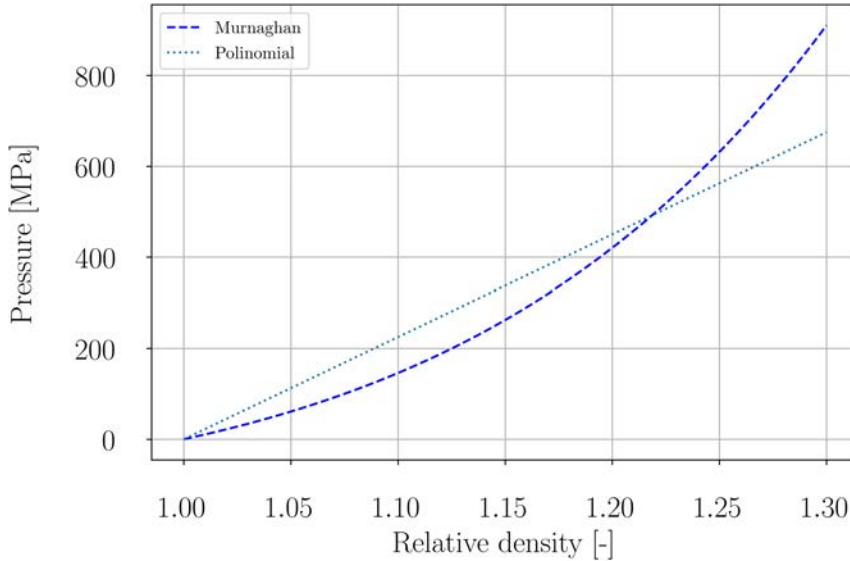


Figure 4: Equation of state used in the numerical simulation

188 slower pressure wave.

189 Finally, contact between the artificial bird and the steel plate (used as a target) was defined by a penalty  
190 contact between the surface of the steel plate and the SPH particles. The interaction between the AB  
191 and the steel plate is achieved by means of a penalty-based node-to-surface contact interface (soft constrain  
192 formulation), implemented within LS-DYNA for dissimilar material properties. In all the contact algorithms,  
193 the SPH particles are considered as nodes. This coupling algorithm prevents the penetration of the nodes  
194 of the AB into the structure mesh applying penalty forces to the AB and the structure. When a particle  
195 of the AB penetrates the Lagrangian structure, a force of recall is applied to both the particle of the AB  
196 and the structural node to make the AB particle return to the surface of the structure avoiding penetration.  
197 The penalty forces are proportional to the penetration depth and penalty stiffness, behaving like a spring  
198 system. As other authors [35, 36] suggest, the contact interface was chosen with special care in order to  
199 achieve the interaction of several SPH particles with each face of the elements of the Lagrange contacting  
200 body.

201 The impact velocity was defined as the velocity measured in the experimental tests setting a initial  
202 velocity to the SPH particles.

203 In order to compare the numerical simulations and the experimental measurements, FEM elements  
204 located analogously as the strain gauges placed in the Hopkinson tube at 350 mm from the impact point  
205 between AB and steel plate were tracked.

## 206 4. Results and discussion

### 207 4.1. Experimental results

208 The analysis of the bird kinematics can be done taking into account the results obtained during the  
209 impact by means of the high speed video cameras, as well as the strain measurements in the Hopkinson  
210 tube. Each of these aspects are discussed in the following sections.

211 Figure 5 shows different frames of an impact of artificial bird against the Hopkinson tube at 120 m/s  
212 from a perspective view. The snap shots were taken at time intervals of 0.1 ms starting at the beginning  
213 of the impact, the last snapshot corresponds to 7 ms after the impact. It can be observed that as soon as  
214 the AB impacts the steel plate, it splatters along the impact plane and starts to flow; similar to a viscous  
215 fluid flowing as a water-jet against a rigid wall. This is consistent with other authors results, which defines  
216 the AB response during the impact as a hydrodynamic behaviour [25]. It can be observed how the artificial  
217 bird flows in an axisymmetric way, with almost a perfect circle shape, similar to a thin disc. The frame  
218 corresponding to 7 ms after the beginning of the impact shows how that thin disc starts to break, due to  
219 the large strain suffered during the impact, and develops radial and circumferential fractures as well as some  
220 AB lumps [9].

221 The velocity evolution of the end of the AB can be obtained from the video images following the back  
222 of the projectile by means of a tracking software. The software is able to follow the projectile until the end  
223 of the AB impacts the Hopkinson tube; the time evolution of different impact birds is depicted in figure  
224 6(a). In this graph the impact velocity was normalized with the initial impact velocity measured by the  
225 laser barriers. Almost in all the cases the laser barriers and the tracking software measure same values, the  
226 tracking method is able to measure the velocity with less than a 10% of error. The velocity at the end of  
227 the projectile remains constant during the impact and presents a decay of around 25% when almost all the  
228 gelatine has impacted. For every impact velocities this sudden decrease presents a similar slope. In addition,  
229 as the impact velocity increases the projectile ends impacts earlier as it is expected. Finally, the data from  
230 Lavoie et al. [25] is included for verification purposes. It is worth to mention that only one type of projectile

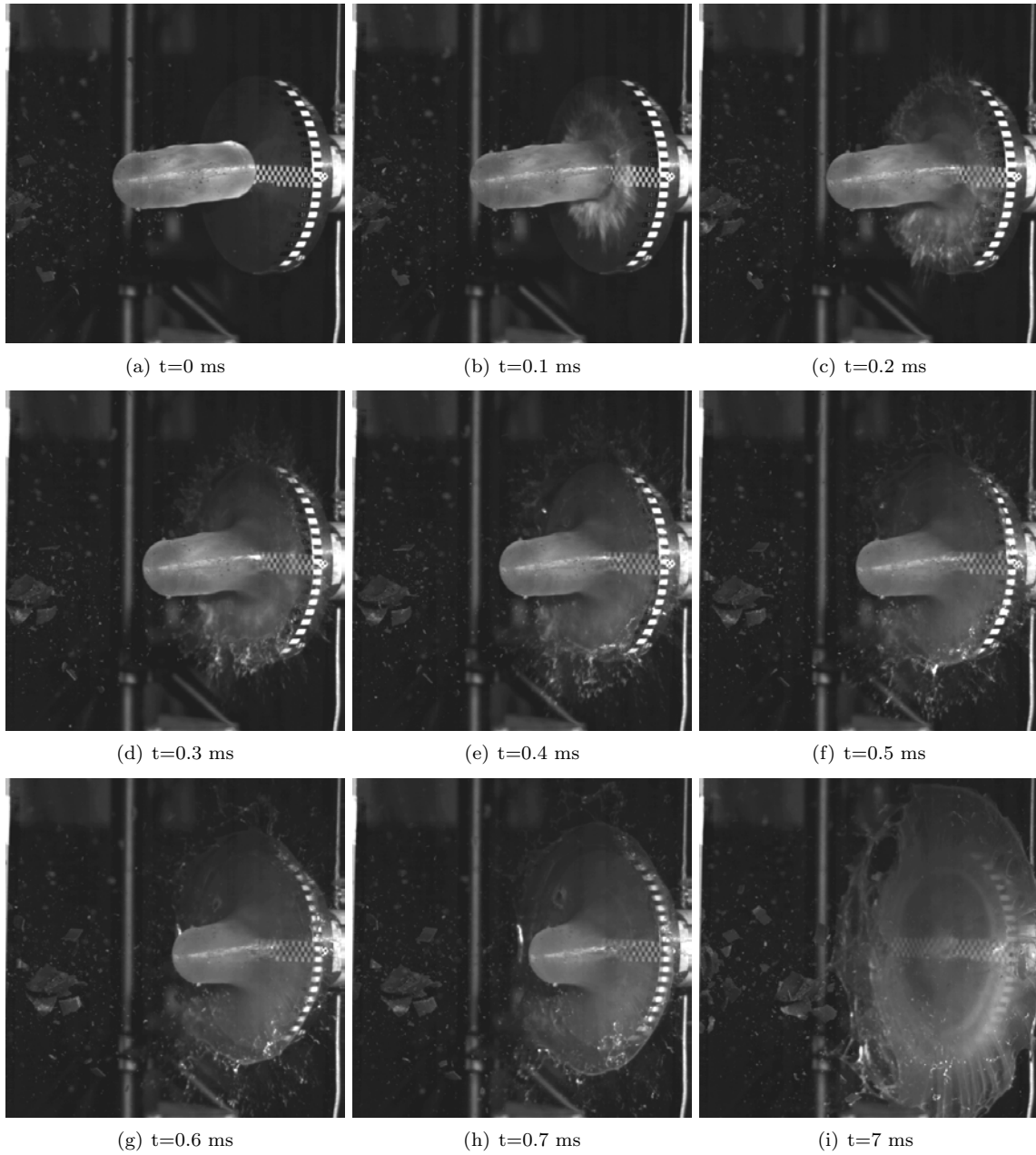
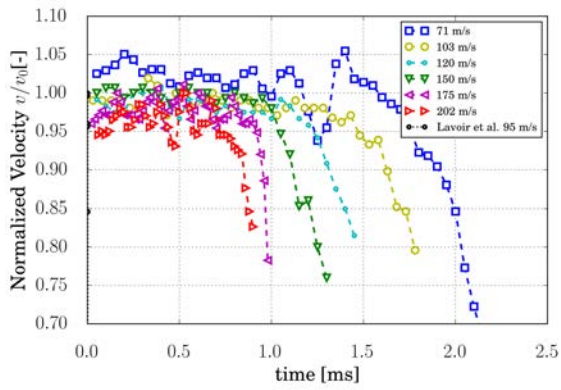


Figure 5: Frames of a test impact at 120 m/s

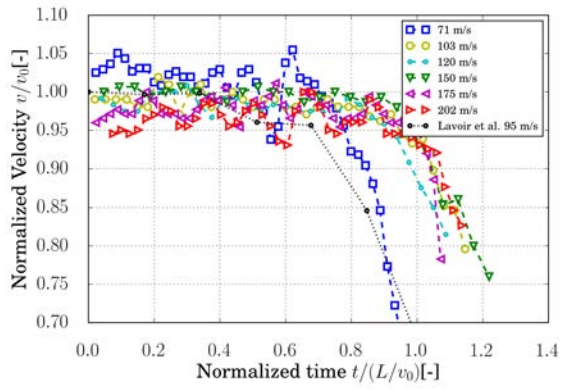
231 and impact velocity ( $95 \text{ m/s}$ ) was considered in that work; in addition the manufacturing process and the  
232 total mass of the AB was different. Nevertheless the results for the same impact velocity follow the same  
233 trend reaching similar values. In figure 6(b) the normalized velocity is plotted against the normalized time  
234 obtained as  $\frac{t}{L/v_0}$ , where  $L$  is the AB length and  $v_0$  is the impact velocity. As it can be seen all the curves  
235 collapse, and start to reduce its value when the normalized time is equal to 1. This could be explained  
236 because at that time the end of the projectile is almost reaching the rigid plate. This confirms that the  
237 deceleration which reach the back of the AB is very low and the effect is concentrated in the impact zone.

238 As well as the velocity time history, the diameter evolution was measured using the images from the  
239 high speed video cameras. Figure 6(c) shows the normalized diameter time evolution. It can be seen that  
240 for all the impact velocities the diameter increases as the AB impacts against the target, as it is expected.  
241 For the lower impact velocities a clear disc formation could be observed and measured in the video images,  
242 but as the impact velocity raises the disc is worst defined and the exterior edge becomes more unsharpened,  
243 making its measurement more difficult. As the diameter reaches between 4 and 5 times the initial diameter  
244 of the projectile, radial cracks could be observed and hence the circle shape is lost (see figure 5(i)). Figure  
245 6(c) also shows that for lower impact velocities ( $70 - 100 \text{ m/s}$ ) the diameter rate raise tends to an horizontal  
246 asymptote; the deformation in these cases is not able to break the gelatine in small pieces or lumps and starts  
247 to recover some of the initial shape: big portions of AB could be recovered after the impact. Nevertheless  
248 for higher impact velocities, this asymptote could not be observed and the projectile breaks in small lumps,  
249 similar behaviour was observed by Allaey et al. [9]. The data from the impact of Lavoie et al. [25] it is also  
250 included. In this case it can be seen more differences for the case between the current test ( $v_0 = 103 \text{ m/s}$ )  
251 and the one of Lavoie et al. ( $v_0 = 95 \text{ m/s}$ ); the reason of this differences can be explained due to the fact  
252 that the aspect ratio is not the same for both cases. In the present case the aspect ratio is  $L/D = 2.8$   
253 whereas in the case of Lavoie et al. is  $L/D = 1.95$ . Therefore lower aspect ratio will produce lower radial  
254 expansion as it is shown. Finally it is also shown the normalized diameter with respect the normalized time  
255 (figure 6(d)). It is observed that in this case the curves do not collapse which means that the radial effect  
256 has not a linear tendency against the impact velocity.

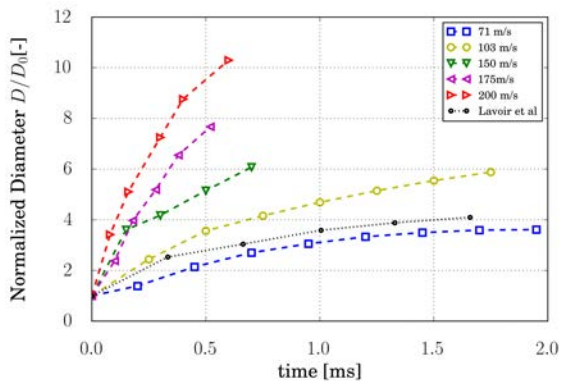
257  
258 This radial expansion can be related mainly with two things: the radial distribution of the induced pres-  
259 sure and the secondary impacts produced by the AB. The portions or lumps formed after the first impact  
260 are deflected at a certain velocity and occasionally could impact to sensible areas. In order to study this  
261 effect it is important to know not only how the projectile is behaving, as it is explained in the previous



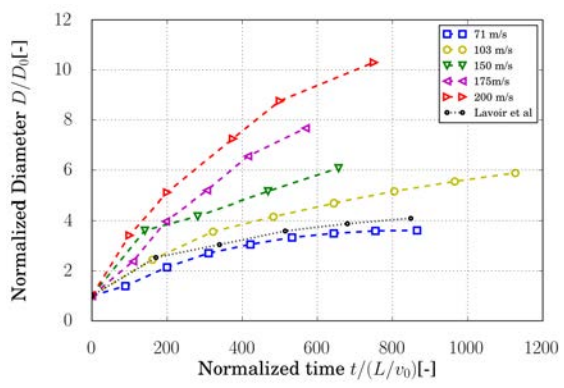
(a) Normalized velocity versus time



(b) Normalized velocity versus normalized time



(c) Normalized diameter versus time



(d) Normalized diameter versus normalized time

Figure 6: Evolution of the impact velocity and AB diameter during the impact for different impact velocities

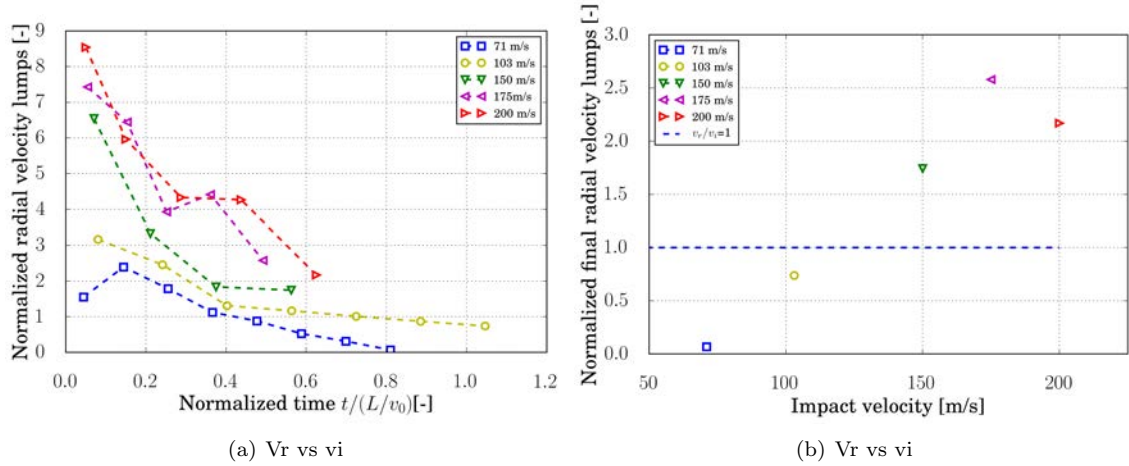


Figure 7: Radial velocity versus impact velocity

262 paragraph, but also the radial velocity of these portions or lumps. This information could be obtained from  
 263 the normalized radial velocity ( $v_{radial}/v_0$ ) showed against the normalized time, figure 7(a). As it can be seen  
 264 for all the cases, the radial velocity shows a maximum and then starts to decrease. The maximum velocity  
 265 reached overcomes the impact velocity. Moreover it can be seen that the relation is not linear and as the  
 266 impact velocity is higher the ratio is even higher. These differences will trigger also variations in the radial  
 267 pressure distribution that depends on the impact velocity. Figure 7(b) depicts the final radial normalized  
 268 velocity as function of the impact velocity, showing an increasing trend with the impact velocity. For the  
 269 slower tests the AB lumps radial velocity barely reaches the initial impact velocity, but in the impacts at  
 270 high velocity ( $v > 150 \text{ m/s}$ ) the smaller size of the exterior lumps (the portions at the outer border of  
 271 the formed disc) reach 2-3 times the initial velocity. Although these lumps have low mass, the high radial  
 272 velocity gives them a high kinetic energy that could be a threat, so further investigation should be done for  
 273 secondary impact which may damage contiguous structural elements.

274  
 275 From the previous results, it can be concluded that the proposed recipe for manufacturing the AB not  
 276 only fulfills the requirements of density, but also behaves in the same manner as artificial birds presented in  
 277 the literature.

278  
 279 From the experimental measurements of the strain gauges in the Hopkinson tube, the strain evolution  
 280 induced by the impact can be obtained. Figure 8 shows, as an example, the strain measured due to a  
 281 artificial bird impact of 355 g impacting at around 120 m/s for 3 different tests. The strain measurements

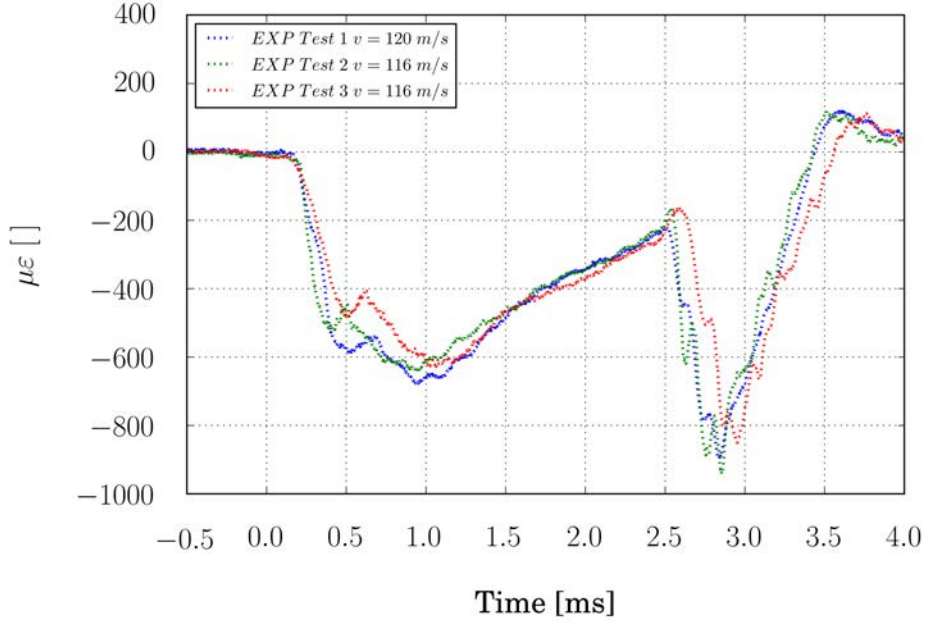


Figure 8: Hopkinson signal for 3 different artificial bird impact test at  $v=120$  m/s mass=355.6 g

282 show a good repeatability for all the impacts, the differences could be related to the variations in the impact  
 283 velocity; similar repeatability could be observed in the other impact velocities tests performed. As soon  
 284 as the compression wave reaches the gauges location, the strain shows a sudden increase until  $\sim 500 \mu\epsilon$ ,  
 285 reaching later the maximum peak at  $\sim 700 \mu\epsilon$  following a gentler slope, this peak is reached in less than a 1  
 286 ms. After this maximum, the strains show a linear decrease until the reflected wave from the opposite face  
 287 of the tube reaches the gauges location. The longitudinal wave speed in the aluminium is  $\sim 5300$  m/s, so  
 288 the wave takes  $\sim 2.25$  ms to travel from one side to another. As it can be seen the second peak ( $\sim 2.75$  ms)  
 289 is higher than the first one, which can be explained because of the combination of the reflected wave and  
 290 the compression pulse that still remains. The reflected wave is a compression pulse because the aluminum  
 291 tube is fixed at its end to a stiffer and high mass steel plate. Later on, the strain decays to almost 0 and  
 292 the measurements oscillate with a damping decay.

293  
 294 Figure 9 presents the values of the strain data obtained for all the impact velocities in which the trend is  
 295 similar to one detailed for previous figure 8. As expected it can be seen that as the impact velocity increases,  
 296 the peak value also increases. It is observed that the peak time tends to decrease as the impact velocity  
 297 increases due to the smaller duration of the impact event in those cases. In figure 9 it is indicated with a  
 298 vertical line the theoretical time in which the impact process occurs ( $t_{th}^{v_i} = \frac{L}{v_i}$  where  $L$  is the length of the AB

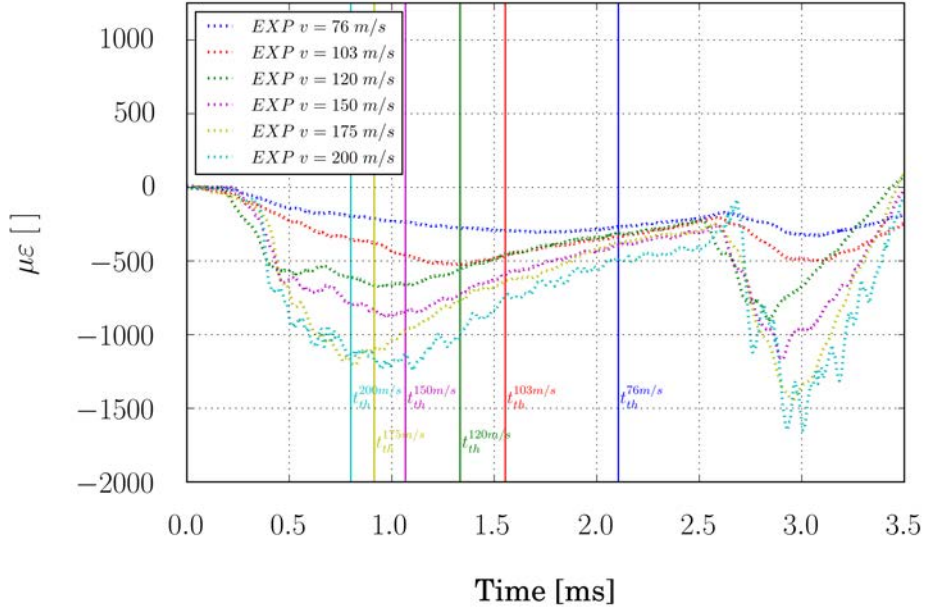


Figure 9: Hopkinson signal for all the impact velocities

299 and  $v_i$  the impact velocity). Similar results of strain measurement have been observed in Tippmann et al. [6].

300

301 Assuming elastic behaviour in the Hopkinson tube, the stress could be obtained for all the impact ve-  
 302 locities. It has been checked that none of the cases reaches the yield stress of the aluminium (for example  
 303 the maximum stress is 105 MPa for the case of 200 m/s). Thus the aforementioned strain values could be  
 304 translated into stress information, and knowing the tube cross section area the force time evolution can be  
 305 obtained. Figure 10 shows the maximum force obtained in the first strain peak (without superposition of  
 306 waves) as a function of the impact velocity. It can be observed that in the range of impact velocities studied  
 307 there is a linear relation between the variables, reaching values of 170 kN for velocities of 200 m/s.

308

## 309 4.2. Comparison with numerical models

### 310 4.2.1. Artificial bird model study

311 As in the experimental results a qualitative comparison with the artificial bird is done. It has to be  
 312 remembered that in this work two different equation of state and two different deviatoric models are used,  
 313 resulting in four different approaches that are used and benchmarked. The four models are named as: Model  
 314 A1 (Fluid like material and polynomial EOS), Model A2 (Fluid like material and Murnaghan EOS), Model  
 315 B1 (Isotropic elastic plastic hydrodynamic material and polynomial EOS) and Model B2 (Isotropic elastic

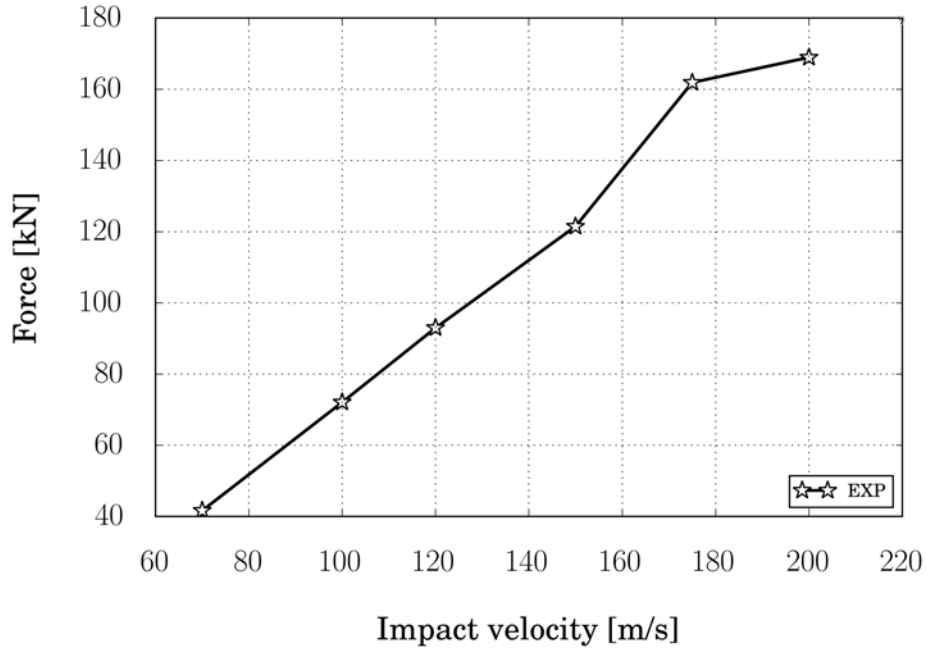


Figure 10: Maximum impact force measured in the Hopkinson tube for all the impact velocities

316 plastic hydrodynamic material and Murnaghan EOS). Figure 11 and 12 show the comparison between the  
 317 experimental impact and the numerical model for 100 m/s and 200 m/s. The numerical model shows a  
 318 proper qualitative comparison regarding the behaviour of the artificial bird. As the bird impacts onto the  
 319 rigid plate it deforms radially at high velocity, phenomenon predicted by all numerical models. It can be  
 320 seen that the differences between the models seem to be negligible for both velocities.

321 Figure 13 shows different frames for an impact of a artificial bird at 120 m/s obtained both experimental  
 322 and numerically. It has been selected the Model A2 (Fluid material with Murnaghan EOS) since all numerical

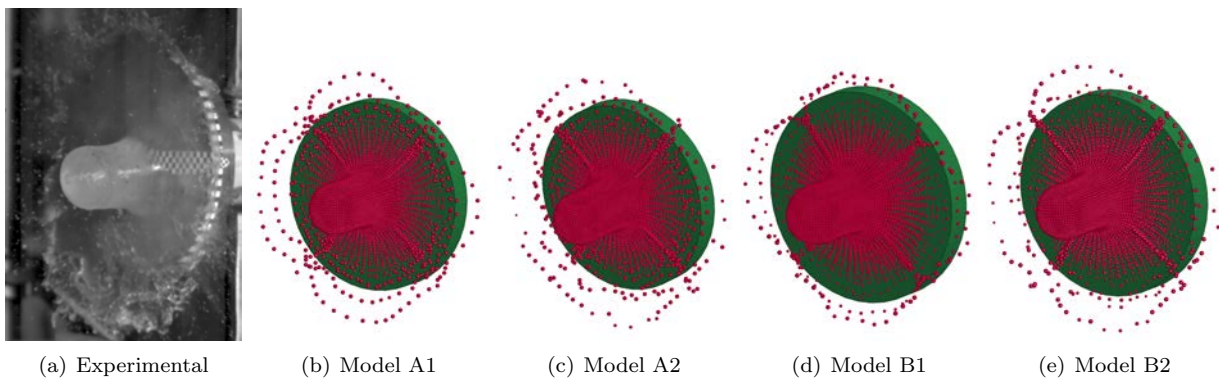


Figure 11: Comparison between the different numerical methods and the experimental results for an impact at 100 m/s at 0.6ms

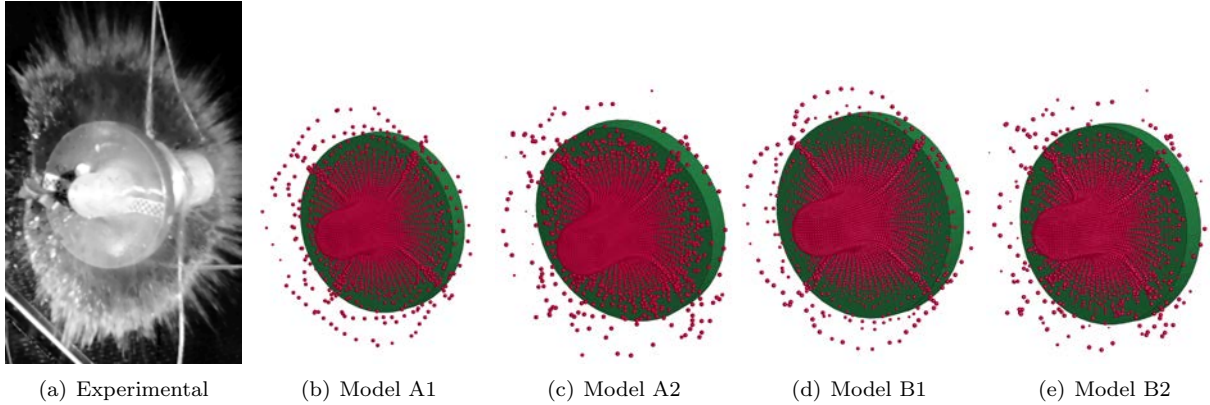


Figure 12: Comparison between the different numerical methods and the experimental results for an impact at 200 m/s at 0.3ms

323 models present similar results. In addition to the lateral images of the numerical simulations, the back images  
 324 of the simulations are included in order to show the evolution of the AB during the impact. The lateral  
 325 images obtained numerically are in agreement with the experimental images, it can be observed that the  
 326 location of the back of the AB in each time is well captured by the numerical model. In addition it could  
 327 be said that the flowing of the bird as well as the partly rebound of the material, against the steel, showing  
 328 a “cloud” in the experimental images is well reproduced by the numerical model. The back images of the  
 329 impact show the evolution of the artificial bird; it can be observed how the material reaches the outer border  
 330 of the steel plate between 0.2 and 0.4 ms in a quasi-circumferential shape.

331 The pressure wave occurs few microseconds after the impact in which a pressure wave generated by  
 332 the impact travels through the gelatin. Due to behaviour is related to the equation of state, the figure 14  
 333 shows the pressures for the fluid-like material and the two different EOS considered (Model A1 and Model  
 334 A2). It can be seen that the pressure wave velocity is slightly higher for the polynomial EOS. This can be  
 335 explained taking into account that pressure wave can be obtained analytically as  $c = \sqrt{\frac{\partial P}{\partial \rho}}$ , and therefore  
 336 it is function of the slope in the pressure-relative density curve (figure 4). In figure 4 can be seen that for  
 337 low relative densities (lower than 1.12), the pressure and the slope is higher for the polynomial EOS. In the  
 338 numerical simulations, for all impact velocities, it can not be seen enough high compression, explaining why  
 339 the pressure wave velocity is higher for this case.

340 From the numerical simulations is also possible to obtain the evolution of the diameter of the AB during  
 341 the impact against the target. In figure 15 it is shown how the diameter evolves in the numerical simulations  
 342 for impacts at 100 and 200 m/s. At the lower velocity it can be seen that up to  $t < 0.5$  ms the numerical  
 343 models reproduces approximately the diameter growing, but after that instant the experimental radial

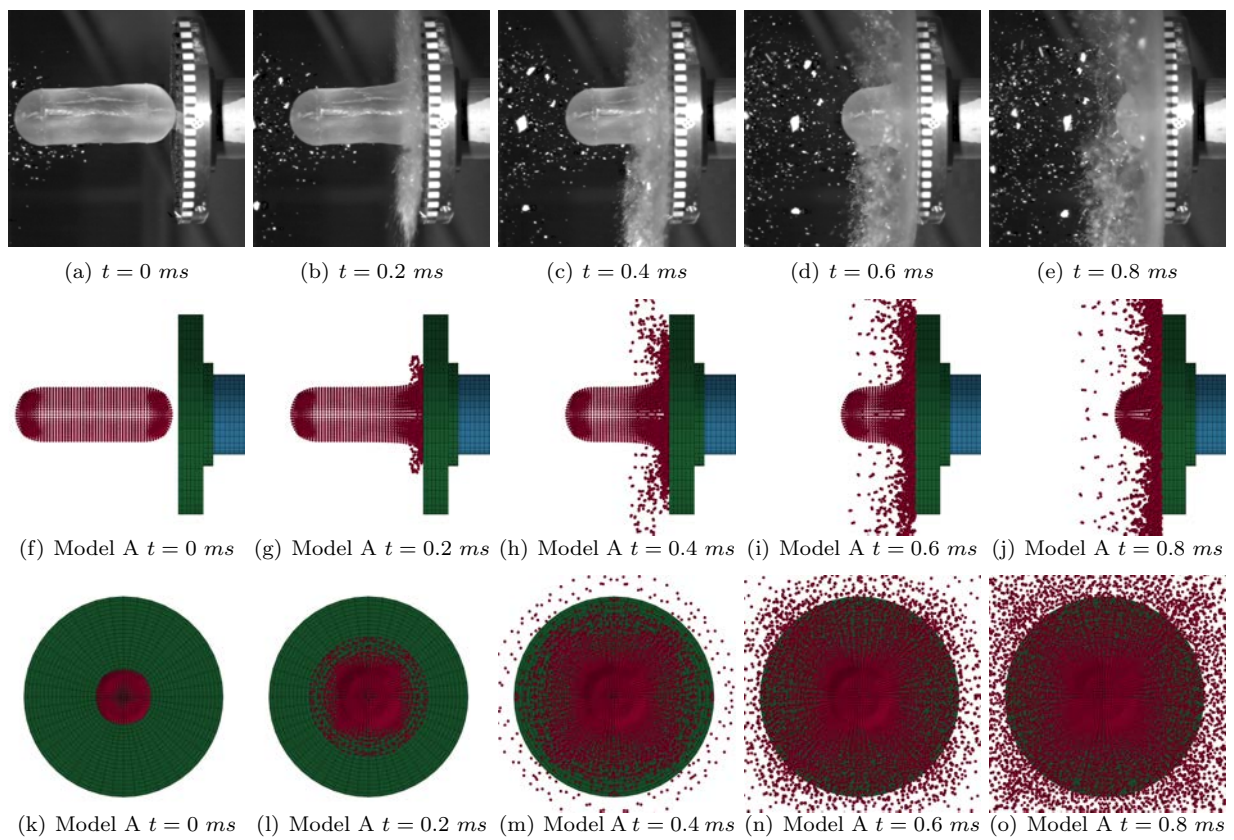


Figure 13: Comparison between the numerical model A2 and the experimental results for an impact at 120 m/s

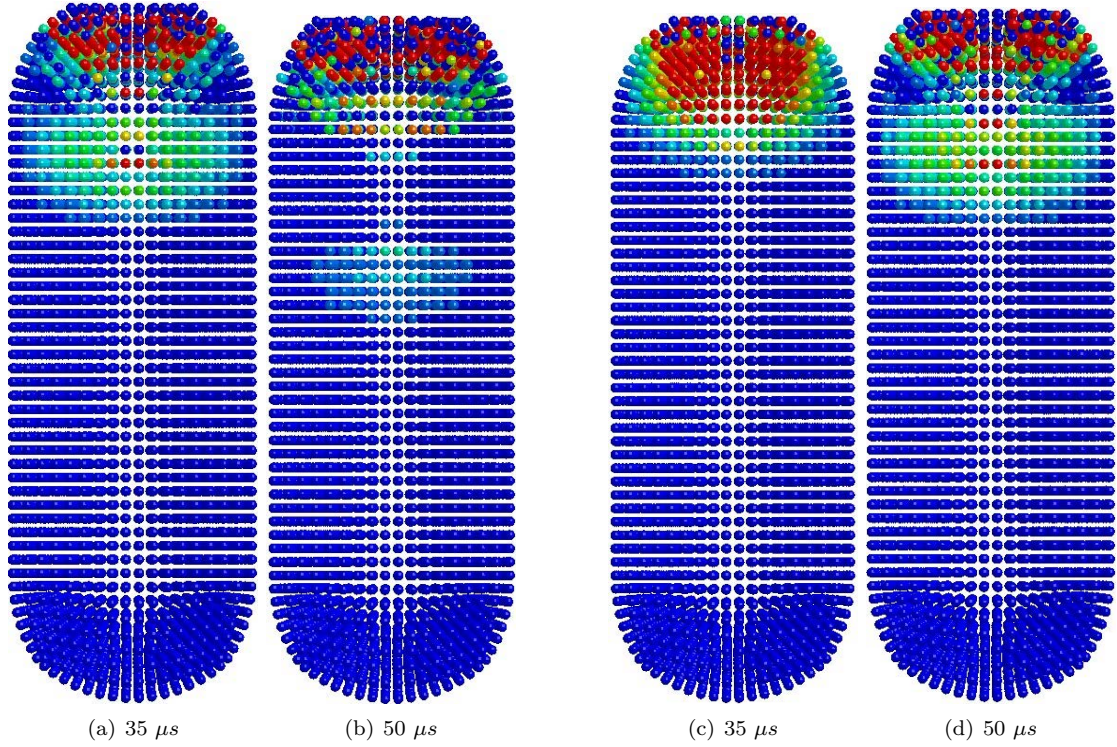


Figure 14: Shock pressures for both Model A1 and A2 (For colour interpretation see the web version of the paper).

344 velocity seems to decrease while in the numerical model remains constant. Due to this effect, all numerical  
 345 models over predict the final diameter. The decrease tendency of the experimental radial velocity could  
 346 be caused by an elastic recovery of the AB, phenomenon that is not seen in the numerical model. Only  
 347 small differences can be seen regarding the diameter growing for all the numerical models: the fluid-like  
 348 material model shows higher radial velocity, while the Murnaghan also shows higher radial velocity than the  
 349 polynomial EOS. For the 200 m/s impact, figure 15 (b), it can be seen that the diameter growing is much  
 350 faster, effect reproduced correctly by the numerical models. For this case the numerical models reproduce  
 351 better the growing of the diameter, although in this case the value is underpredicted for  $t < 0.5$  ms. As in  
 352 the previous case, it can be seen that the experimental radial velocity starts to decrease while, this effect is  
 353 not seen in the numerical models. Also small differences can be seen for the 4 numerical models. Although  
 354 in this case, the polynomial EOS shows higher velocity than the Murnaghan EOS. The differences observed  
 355 in comparison with the experimental results could be related to the incapacity of the numerical models to  
 356 reproduce the elastic recovery of the projectile. As have been observed in figures 11 and 12, the numerical  
 357 model behaves similar at both velocities but the experimental images show a difference at the outer border  
 358 of the radial expansion of the projectile. At 100 m/s the AB radial border is starting to form the big lumps

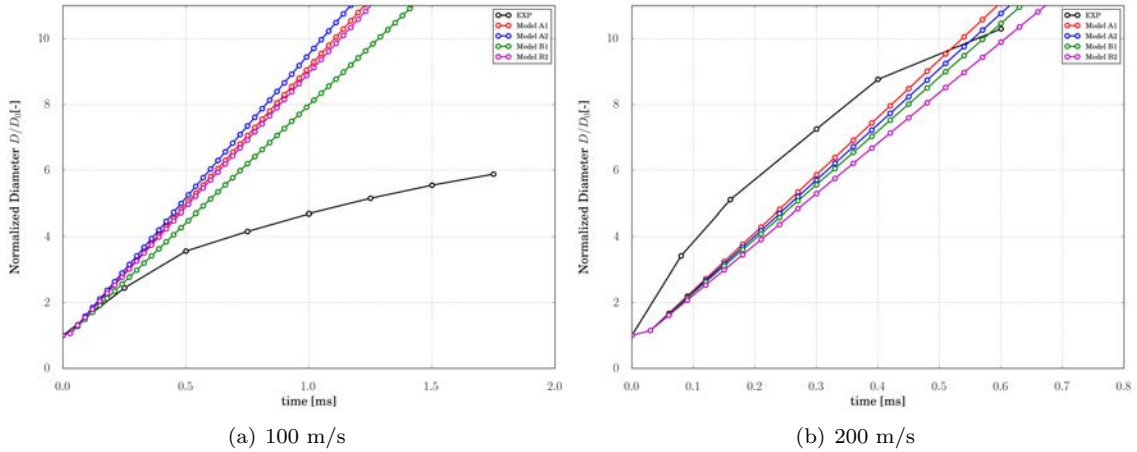


Figure 15: Predicted diameter evolution for 2 different impact velocities

359 observed, whereas at 200 m/s the radial border shows a more fluid behavior as the simulations predict. Thus  
 360 the normalize diameter is better predicted by the numerical model at high impact velocity.

361 In figure 16 it has been obtained the normalized radial velocity for the impacts at 100 m/s and 200  
 362 m/s for the experimental impact and only one numerical model, since differences between numerical models  
 363 are negligible. It can be seen that the experimental curves show differences between both velocities, while  
 364 in the numerical curves the normalized radial velocity is similar for both. Also the numerical models do  
 365 not show the decrease tendency of radial velocity with time. Therefore, other material behavior would be  
 366 desirable to use for modelling more precisely the radial expansion of the AB at the different range of velocities.

367

#### 368 4.2.2. Hopkinson tube model study

369 In order to study the effects that the different AB models considered may induce due to the impact, the  
 370 stress and force withstand by the hopkinson tube are analyzed. Figure 17 shows the comparison between the  
 371 stress obtained where the strain gauges were located in the experiments and in the analogous elements of the  
 372 simulations. All the numerical approaches predict similar results in terms of stress in the Hopkinson tube  
 373 and therefore it can be established that all the proposed models produce similar contact forces. Consequently  
 374 the differences in the deviatoric behaviour and in the equation of state used for the models in the literature  
 375 does not affect to the compression force produced by the impact. Due to differences between the models  
 376 are negligible it can be established that the effect of a AB event is mainly controlled by the momentum  
 377 transmission. Also it can be seen that the trend is well predicted by the numerical models considered:  
 378 the first slope reaching the maximum stress of the compression pulse, the linear decay and finally the

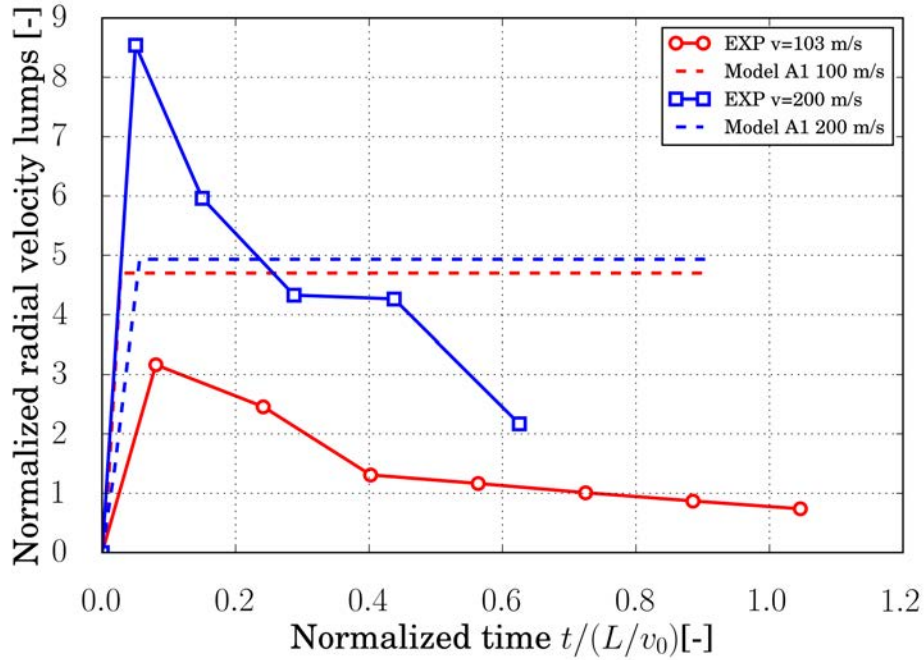
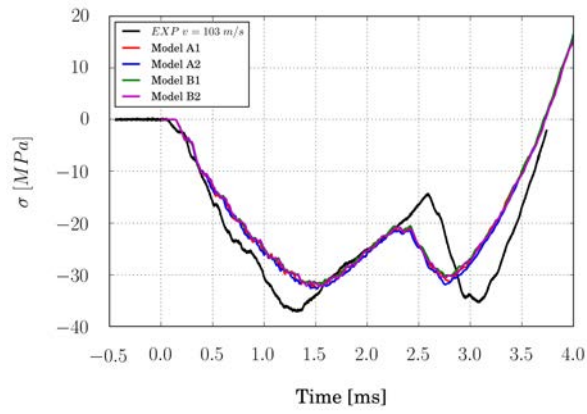


Figure 16: Experimental and numerical normalized radial velocity versus normalized time at 100 and 200 m/s

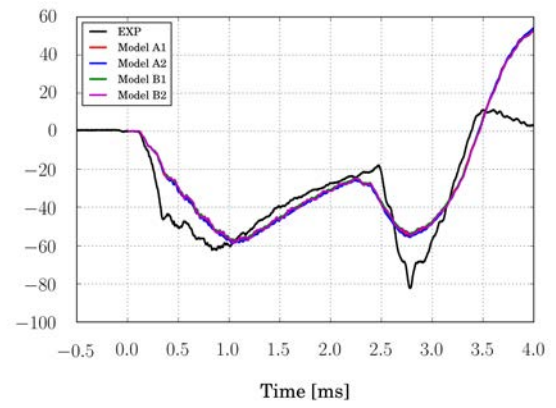
379 superposition of waves giving as result a higher stress peak. The time to the maximum peak predicted in  
 380 all the cases is a little bit delayed because the slope in the experimental results are steeper, this is more  
 381 evident as the impact velocity is increased. The decay slope is well captured but the time of arrival for the  
 382 2nd compression wave to arrive at the strain gauges location is shorter in the numerical simulations. This  
 383 could be explained because the numerical simulations idealize the tied contact between the different parts of  
 384 the Hopkinson tube and the waves are reflected in an ideal way. Finally the numerical simulations predict  
 385 an additional tensile pulse ( $t > 3.5$  ms). This could be produced because of the contacts between the tube  
 386 and the steel plates: in the experimental setup it is observed that the parts start to separate slightly after  
 387 the tension wave, trapping the pulse [37].

388 From the measurements of the stress in the numerical simulations the maximum force of the impact  
 389 could be obtained and compared with the experimental results, figure 18 shows the predicted maximum  
 390 force values for all the range of velocities. All the numerical approaches predict similar values of peak force.  
 391 As it was previously concluded the impact event effects are controlled by the momentum transfer and the  
 392 material model differences are negligible for the Hopkinson tube data. The increase trend with the impact  
 393 velocity is faithfully predicted by the numerical simulations

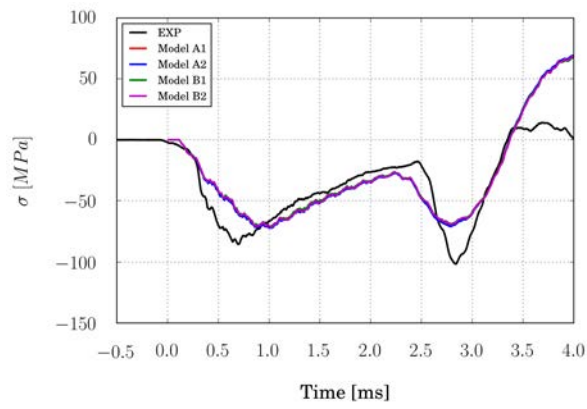
394 Finally, from the surface in contact between the projectile and the Hopkinson tube it can be obtained



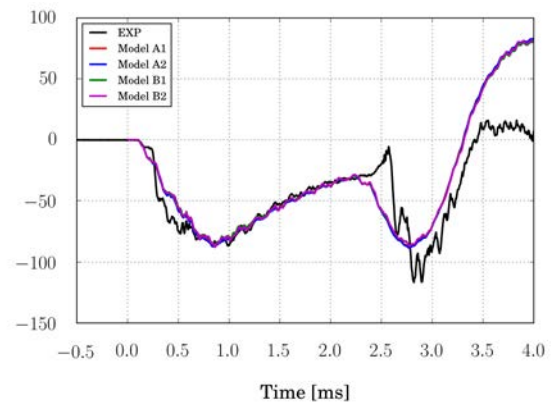
(a) 100 m/s



(b) 150 m/s



(c) 175 m/s



(d) 200 m/s

Figure 17: Comparison between experimental and numerical results measured in the Hopkinson tube

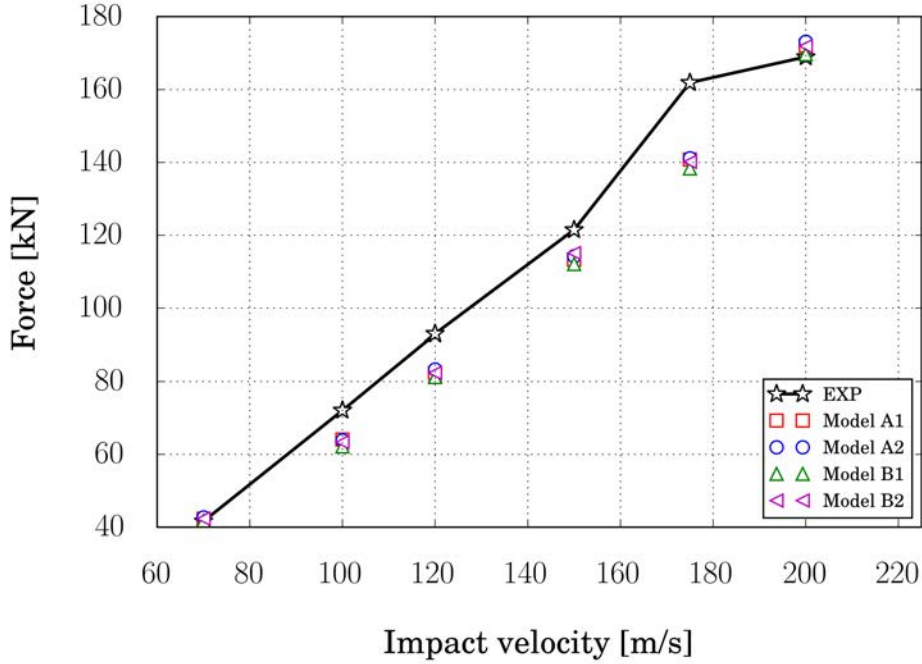


Figure 18: Maximum impact force measured in the Hopkinson tube for all the impact velocities for both numerical approaches

395 the contact force exerted by the artificial bird against the steel target. Figure 19 shows the contact force  
 396 obtained from the numerical models and compared with the theoretical stagnation force ( $F = \frac{mv^2}{L}$ ) [38].  
 397 As it was seen before the differences between the models are small, so only two approaches are presented in  
 398 which deviatoric behaviour and EOS are different (model A2 and model B1). It can be observed how both  
 399 numerical approaches predict a first peak followed by a steady state force, which is similar to the theoretical  
 400 value of the stagnation force. If the impulse is obtained for both curves it can be seen that both values  
 401 are very similar between them ( $I_{A2} = 53.4 \text{ Ns}$  and  $I_{B1} = 50.2 \text{ Ns}$ ), and also to the AB initial momentum  
 402 ( $m_{AB} v = 52.5 \text{ Ns}$ )

403

## 404 5. Conclusions

405 It is presented a novel impact test campaign in artificial bird impact in a wide range of velocities,  
 406 measuring the force induced by the impact using a 1-D facility (Hopkinson tube). Moreover, is presented  
 407 a simplified ‘recipe’ for the artificial bird, which works in accordance with the observation of other authors  
 408 and respect the densities and dimensions measured in different bird species. The behaviour of the AB is  
 409 measured and monitored during the impact using high speed video cameras and the induced strain measured

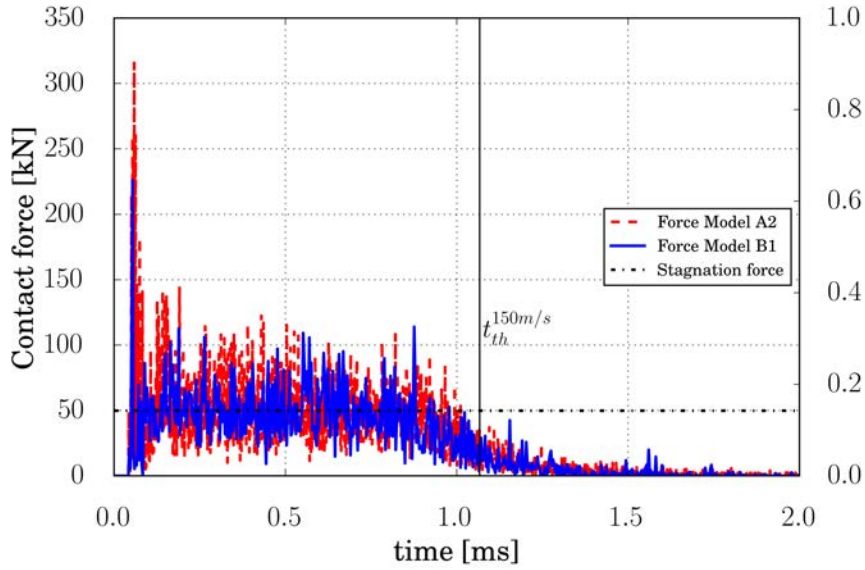


Figure 19: Contact force history for an impact at 150 m/s

410 using a data acquisition system. From the experimental campaign could be concluded:

- 411 • The behaviour of the artificial bird with the simplified recipe follows the observation of different  
412 authors, behaving as a fluid-like material.
- 413 • The experimental setup allows to measure the kinematics of the artificial bird, in this case, the projectile  
414 deceleration and radial expansion has been successfully obtained. It can be seen that at high velocities  
415 ( $v > 125 \text{ m/s}$ ) the radial velocity reaches higher values than the initial impact velocity.
- 416 • The proposed force measurement using a Hopkinson tube produces straight forward results to be used  
417 as a benchmarking for numerical models of soft (highly deformable) impactors. It can be seen that  
418 the maximum impact force increases linearly with the impact velocity as it is expected.

419 All the data extracted from the experimental test are valuable measurements for validation purposes of  
420 other researchers and they are shared in the present article.

421  
422 In addition to the experimental campaign, the article presents an extensive numerical analysis. The  
423 authors use four different numerical approaches taken from the literature and compare the numerical simu-  
424 lations with the experimental results. From the numerical work could be concluded:

- 425 • Numerical approaches are capable to reproduce the projectile kinematics during the impact, but models  
426 predicts less accurately the radial expansion, especially at lower impact velocities. Improvements in

427 the material models would be desirable to use for modelling more precisely the radial expansion of the  
428 AB at the different range of velocities. Further investigations regarding influence of secondary impact  
429 and pressure distribution should also be accomplished.

- 430 • All the numerical models reproduce faithfully the strain/stress histories obtained in the Hopkinson  
431 tube, not only the peak values but also the measured trends.
- 432 • Differences between numerical models have been proved to be negligible, both in the normal contact  
433 force and radial expansion. This could indicate that the AB impact process is mainly governed by the  
434 momentum transfer.

435 Future experimental work will involve an investigation of the impact angle influence and a secondary  
436 impact measurement. In order to be capable of provide information and clarify the force and momentum in  
437 this secondary impact. From this experimental data a further investigation and bechmarking of the numerical  
438 approaches could lead to a better understanding of the artificial bird behaviour during the impact.

#### 439 **Acknowledgements**

440 This research was done with the financial support of the mobility intern-ship for researchers of Carlos III  
441 University of Madrid (Spain) (“Programa propio de investigación - Convocatoria 2014 movilidad”) and the  
442 Vicerrectorado de Política Científica project 2014/00006/002 and 2013/00413/003. Also the authors want  
443 to acknowledge the University of Edinburgh for its support in the research stays.

#### 444 **References**

- 445 [1] J. A. Toso N, LIBCOS-Load upon impact behaviour of composite Structure Research Project EASA.2009/3, Tech. rep.,  
446 European Aviation Safety Agency (2011).
- 447 [2] G. J. Appleby-Thomas, P. J. Hazell, G. Dahini, On the response of two commercially-important CFRP structures to  
448 multiple ice impacts, *Compos. Struct.* 93 (10) (2011) 2619–2627.
- 449 [3] W. Cantwell, J. Morton, Comparison of the low and high velocity impact response of cfrp, *Composites* 20 (1989) 545–51.
- 450 [4] J. Rhymer, H. Kim, D. Roach, The damage resistance of quasi-isotropic carbon/epoxy composite tape laminates impacted  
451 by high velocity ice, *Composites Part A* 43 (7) (2012) 1134–1144.
- 452 [5] J. Pernas-Sánchez, J. A. Artero-Guerrero, D. Varas, J. López-Puente, Analysis of ice impact process at high velocity, *Exp.*  
453 *Mech.* 55 (9) (2015) 1669–1679.
- 454 [6] J. D. Tippmann, H. Kim, J. D. Rhymer, Experimentally validated strain rate dependent material model for spherical ice  
455 impact simulation, *International Journal of Impact Engineering* 57 (Supplement C) (2013) 43 – 54.
- 456 [7] J. S. Wilbeck, Impact behavior of low strength projectiles., Tech. rep., Air Force Materials Laboratory (1977).

- 457 [8] D. Nandlall, A. Gakwaya, On the determination of the shock and steady state parameters of gelatine from cylinder impact  
458 experiments, *International Journal of Impact Engineering* 116 (2018) 22 – 33.
- 459 [9] F. Allaey, G. Luyckx, W. V. Paepegem, J. Degrieck, Characterization of real and substitute birds through experimental  
460 and numerical analysis of momentum, average impact force and residual energy in bird strike on three rigid targets: A  
461 flat plate, a wedge and a splitter, *International Journal of Impact Engineering* 99 (Supplement C) (2017) 1 – 13.
- 462 [10] J. D. Seidt, J. M. Pereira, J. T. Hammer, A. Gilat, *Dynamic Load Measurement of Ballistic Gelatin Impact Using an*  
463 *Instrumented Tube*, Springer New York, New York, NY, 2013, Ch. 31, pp. 243–250.
- 464 [11] J. Liu, Y. Li, X. Yu, Z. Tang, X. Gao, J. Lv, Z. Zhang, A novel design for reinforcing the aircraft tail leading edge structure  
465 against bird strike, *International Journal of Impact Engineering* 105 (Supplement C) (2017) 89 – 101, *design and Analysis*  
466 *of Protective Structures* 2015.
- 467 [12] D. Hu, B. Song, D. Wang, Z. Chen, Experiment and numerical simulation of a full-scale helicopter composite cockpit  
468 structure subject to a bird strike, *Composite Structures* 149 (Supplement C) (2016) 385 – 397.
- 469 [13] J. Liu, Y. Li, X. Gao, Bird strike on a flat plate: Experiments and numerical simulations, *International Journal of Impact*  
470 *Engineering* 70 (Supplement C) (2014) 21 – 37.
- 471 [14] J. Lacombe, Smoothed particle hydrodynamics method in LS-DYNA, in: 3rd German LS-DYNA forum, Bamberg, Germany,  
472 2004.
- 473 [15] A. Zammit, M. Kim, J. Bayandor, Bird-strike damage tolerance analysis of composite turbofan engines, in: ICAS 2010,  
474 27th international Congress of the Aeronautical Sciences, Nice, France, 2010.
- 475 [16] M. Anghileri, L. Castelletti, F. Invernizzi, M. Mascheroni, Birdstrike onto the composite intake of a turbofan engine, in:  
476 5th European LS-DYNA User's Conference, Birmingham, UK, 2005.
- 477 [17] J. Liu, Y. Li, F. Xu, The numerical simulation of a bird-impact on an aircraft windshield by using the SPH method,  
478 *Advanced Materials Research* 33–37 (2008) 851–85–6.
- 479 [18] S. Georgiadis, A. Gunnion, R. Thomson, B. Cartwright, Bird-strike simulation for certification of the Boeing 787 composite  
480 moveable trailing edge, *Composite Structures* 86 (2008) 258–2–68.
- 481 [19] L. Wu, Y. Guo, Y. Li, Bird strike simulation on sandwich composite structure of aircraft radome, *Explosion and Shock*  
482 *Waves* 29 (2009) 642–64–7.
- 483 [20] H. Salehi, S. Ziaei-Rad, M. Vaziri-Zanjani, Bird impact effects on different types of aircraft bubble windows using numerical  
484 and experimental methods, *International Journal of Crashworthiness* 15 (2010) 93–106.
- 485 [21] A. Riccio, R. Cristiano, S. Saputo, A. Sellitto, Numerical methodologies for simulating bird-strike on composite wings,  
486 *Composite Structures* 202 (2018) 590 – 602, special issue dedicated to Ian Marshall.
- 487 [22] M. Siemann, S. Ritt, Novel particle distributions for sph bird-strike simulations, *Computer Methods in Applied Mechanics*  
488 *and Engineering* 343 (2019) 746 – 766.
- 489 [23] D. Hamershock, T. Seamans, G. Bernhardt, Determination of body density for twelve bird species, Tech. rep., Wright  
490 Laboratory (1993).
- 491 [24] R. Budgey, The development of a substitute artificial bird by the international birdstrike research group for use in aircraft  
492 component testing., Tech. rep., INTERNATIONAL BIRD STRIKE COMMITTEE (2000).
- 493 [25] M. Lavoie, A. Gakwaya, M. Nejad-Ensan, D. Zimcik, D. Nandlall, Bird's substitute tests results and evaluation of available  
494 numerical methods, *International Journal of Impact Engineering* 36 (10) (2009) 1276 – 1287.
- 495 [26] F. D. Caprio, D. Cristillo, S. Saputo, M. Guida, A. Riccio, Crashworthiness of wing leading edges under bird impact event,

- 496 Composite Structures 216 (2019) 39 – 52.
- 497 [27] R. Hedayati, S. Ziaei-Rad, A new bird model and the effect of bird geometry in impacts from various orientations,  
498 Aerospace Science and Technology 28 (1) (2013) 9 – 20.
- 499 [28] Z. Zhang, L. Li, D. Zhang, Effect of arbitrary yaw/pitch angle in bird strike numerical simulation using sph method,  
500 Aerospace Science and Technology 81 (2018) 284 – 293.
- 501 [29] J. J. Monaghan, Smoothed particle hydrodynamics, Annual Review of Astronomy and Astrophysics 30 (1) (1977) 543–574.
- 502 [30] H. Ren, X. Zhuang, T. Rabczuk, Dual-support smoothed particle hydrodynamics in solid: variational principle and implicit  
503 formulation (2018). arXiv:1810.06010.
- 504 [31] S. Jenq, F. Hsiao, I. Lin, D. Zimcik, M. N. Ensan, Simulation of a rigid plate hit by a cylindrical hemi-spherical tip-ended  
505 soft impactor, Computational Materials Science 39 (3) (2007) 518 – 526.
- 506 [32] R. Vignjevic, M. Orłowski, T. D. Vuyst, J. C. Campbell, A parametric study of bird strike on engine blades, International  
507 Journal of Impact Engineering 60 (Supplement C) (2013) 44 – 57.
- 508 [33] V. Nagaraj, T. Velmurugan, Numerical bird strike impact simulation of aircraft composite structure, Journal of Mechanical  
509 and Civil Engineering 01–10.
- 510 [34] M. A. McCarthy, J. R. Xiao, C. T. McCarthy, A. Kamoulakos, J. Ramos, J. P. Gallard, V. Melito, Modelling of bird strike  
511 on an aircraft wing leading edge made from fibre metal laminates – part 2: Modelling of impact with sph bird model,  
512 Applied Composite Materials 11 (5) (2004) 317–340.
- 513 [35] J. Xu, J. Wang, Interaction methods for the sph parts (multiphase flows, solid bodies) in ls-dyna, in: 13th International  
514 LS-DYNA User’s Conference, Detroit, 2014.
- 515 [36] L. Schwer, Preliminary assessment of non-lagrangian methods for penetration simulation, in: 8th International LS-DYNA  
516 User’s Conference, Detroit, 2004.
- 517 [37] S. Nemat-Nasser, J. Isaacs, J. E. Strett, Hopkinson techniques for dynamic recovery experiments, Proceedings of the  
518 Royal Society of London A: Mathematical, Physical and Engineering Sciences 435 (1894) (1991) 371–391.
- 519 [38] S. Abrate, Soft impacts on aerospace structures, Progress in Aerospace Sciences 81 (2016) 1 – 17, dynamic Loading Aspects  
520 of Composite Materials.